# Simultaneous Dual-Doppler and Mobile Mesonet Observations of Streamwise Vorticity Currents in Three Supercells

SHAWN S. MURDZEK, PAUL M. MARKOWSKI, AND YVETTE P. RICHARDSON

<sup>a</sup> Department of Meteorology and Atmospheric Science, The Pennsylvania State University, University Park, Pennsylvania

(Manuscript received 20 July 2020, in final form 25 September 2020)

ABSTRACT: Recent high-resolution numerical simulations of supercells have identified a feature referred to as the streamwise vorticity current (SVC). Some have presumed the SVC to play a role in tornadogenesis and maintenance, though observations of such a feature have been limited. To this end, 125-m dual-Doppler wind syntheses and mobile mesonet observations are used to examine three observed supercells for evidence of an SVC. Two of the three supercells are found to contain a feature similar to an SVC, while the other supercell contains an antistreamwise vorticity ribbon on the southern fringe of the forward flank. A closer examination of the two supercells with SVCs reveals that the SVCs are located on the cool side of boundaries within the forward flank that separate colder, more turbulent flow from warmer, more laminar flow, similar to numerical simulations. Furthermore, the observed SVCs are similar to those in simulations in that they appear to be associated with baroclinic vorticity generation and have similar appearances in vertical cross sections. Aside from some apparent differences in the location of the maximum streamwise vorticity between simulated and observed SVCs, the SVCs seen in numerical simulations are indeed similar to reality. The SVC, however, may not be essential for tornadogenesis, at least for weak tornadoes, because the supercell that did not have a well-defined SVC produced at least one brief, weak tornado during the analysis period.

KEYWORDS: Tornadogenesis; Mesocyclones; Severe storms; Supercells; Tornadoes; Radars/Radar observations

#### 1. Introduction

Tornado research has focused primarily on tornadogenesis within supercell thunderstorms owing to the fact that supercells produce a disproportionate number of significant tornadoes. Tornadogenesis within supercells can be conceptualized as a three-step process (e.g., Davies-Jones 2015). First, midlevel rotation develops from the tilting of environmental horizontal vorticity (Rotunno 1981). Second, vertical vorticity develops close to the surface (the tornado "seed," e.g., Dahl 2015). Third, this near-surface<sup>2</sup> vertical vorticity is intensified via stretching into a tornado-strength vortex. Steps 2 and 3 are sensitive to internal features within supercells and are examined in more detail below.

The formation of the tornado seed requires the presence of a downdraft to transport circulation-rich air toward the surface (e.g., Davies-Jones and Brooks 1993). Parcels destined for the tornado seed have been shown to gain considerable horizontal vorticity owing to baroclinic generation (Klemp and Rotunno 1983; Rotunno and Klemp 1985; Dahl et al. 2014; Dahl 2015). Continuous baroclinic generation of horizontal vorticity as parcels descend in downdrafts may result in the vorticity vector developing a crosswise component in the vertical, with the outcome that positive vertical vorticity develops near the nadir of the parcel trajectory (Davies-Jones and Brooks 1993). The

Corresponding author: Shawn S. Murdzek, smurdzek@psu.edu

generation of near-surface vertical vorticity appears to be facilitated by kinematic boundaries within the forward flank of supercells that form when cold downdraft outflow collides with relatively warmer modified inflow. In particular, numerical simulations have found that parcels destined for the tornado seed collect along boundaries that are collocated with prominent horizontal buoyancy gradients, forming "rivers" of vertical vorticity in the lowest few hundred meters that feed the tornado-like vortex (Dahl et al. 2014; Coffer and Parker 2017). In regards to tornado prediction, Coffer and Parker (2018) suggest that most supercells can develop sufficient near-surface vertical vorticity and that the limiting factor is whether the tornado seed can be stretched into a tornado-strength vortex by the parent supercell (i.e., step 3).

The stretching of near-surface vertical vorticity is thought to be facilitated by the low-level mesocyclone. The rotation within the low-level mesocyclone is associated with dynamic pressure falls, which result in an upward-pointing vertical perturbation pressure gradient force (VPPGF) that can lift near-surface parcels from beneath the low-level mesocyclone (Coffer and Parker 2017). Low-level mesocyclonic rotation results from the tilting and stretching of vorticity that is initially horizontal, with increasing amounts of streamwise vorticity ( $\omega_s$ ) resulting in a greater collocation between the vertical vorticity and vertical velocity maxima (Davies-Jones 1984), where  $\omega_s$  is defined in a storm-relative sense:

$$\omega_s = \frac{(\mathbf{v} - \mathbf{c}) \cdot (\nabla \times \mathbf{v})}{|\mathbf{v} - \mathbf{c}|},\tag{1}$$

where **v** and **c** are the wind velocity and storm motion vectors, respectively. Aligned with the theoretical results from Davies-Jones (1984), increasing amounts of low-level environmental

<sup>&</sup>lt;sup>1</sup>≥EF2, where "EF" refers to the enhanced Fujita scale.

<sup>&</sup>lt;sup>2</sup> Following Murdzek et al. (2020), "near-surface" is defined as the lowest 50 m whereas "low-level" refers to altitudes below 1000 m.

TABLE 1. Overview of the three VORTEX2 cases examined in this article. "Date" refers to the date the storm formed, so for the Maysville and La Junta storms, the dates that correspond to the listed time intervals are actually 8 and 12 Jun, respectively.

Date	Location	Analysis times (UTC)	Baseline (km)	References
7 Jun 2009	Maysville, MO	0054-0134	6.4	This article
11 Jun 2009	La Junta, CO	0000-0032	11.8	Atkins et al. (2014)
26 May 2010	Prospect Valley, CO	2218–2302	9.9	Tanamachi et al. (2013); Bowlan (2013); Murdzek et al. (2020)

 $\omega_s$  have been found to contribute to stronger and more organized low-level mesocyclones that are more likely to instigate tornadogenesis (Coffer and Parker 2017; Coffer et al. 2017; Coffer and Parker 2018). This is further supported by the observation that tornadic supercell environments generally possess larger amounts of storm-relative helicity (SRH; Davies-Jones et al. 1990), compared to nontornadic supercell environments (Rasmussen 2003; Thompson et al. 2003; Coffer et al. 2019). This suggests that at least some of the horizontal vorticity destined for the low-level mesocyclone is imported from the environment.

Recent high-resolution numerical simulations have suggested that storm-generated baroclinic horizontal vorticity may also contribute to low-level mesocyclone intensification. A 30-m simulation by Orf et al. (2017) identified a feature they referred to as the streamwise vorticity current (SVC), which is a "tube" of streamwise horizontal vorticity that develops within the forward flank and feeds the low-level mesocyclone. In Orf et al.'s simulation, an intensification of the SVC led to a stronger low-level mesocyclone with larger dynamic pressure falls, which resulted in tornadogenesis owing to a stronger VPPGF (Orf et al. 2018). Similar to the development of the tornado seed, the SVC is coupled with boundaries within the forward and left flanks of the supercell.<sup>3</sup> The SVC in Orf et al. (2017), as well as in other simulations (e.g., Schueth 2018; Finley et al. 2018), occurs on the immediate cool side of a boundary within the forward flank. The strong horizontal buoyancy gradients often associated with these boundaries are thought to augment the streamwise horizontal vorticity within the SVC through the baroclinic generation of horizontal vorticity (Schueth 2018), which suggests that stronger horizontal buoyancy gradients may result in a stronger SVC and therefore a stronger low-level mesocyclone (Schueth and Weiss 2020). It is worth noting that the idea that storm-generated horizontal vorticity contributes to the low-level mesocyclone is not new; this idea has been around since at least the 1980s (Rotunno and Klemp 1985). What is new is that this baroclinic vorticity generation can be visualized using highresolution simulations as a relatively narrow, intense ribbon of streamwise horizontal vorticity (Weiss et al. 2020) and that variations in the strength of the SVC can be tied to the strength of the low-level mesocyclone, and, therefore, tornado genesis and maintenance.

The majority of research related to SVCs to date has been performed using idealized numerical models. Therefore, before further research is done into the connection between SVCs and tornadogenesis, it is necessary to determine whether the SVC exists in observed supercells and start documenting the range of SVC characteristics in order to assess the realism of modelgenerated SVCs. Some work has already been done in this area. Most notably, the Texas Tech mobile Ka-band radars have been used to probe the forward flank of supercells using range-height indicators (RHIs) to verify the presence of the SVC. Schueth (2018) and Schueth and Weiss (2018) present RHI scans from two different supercells that contain a feature similar in appearance to a Kelvin-Helmholtz billow in the forward flank that bears a strong resemblance to synthetic RHIs through the SVC of a simulated supercell. Preliminary results from the 2019 field campaign of the Targeted Observations by Radars and UAS of Supercells (TORUS; Houston et al. 2020) also show evidence of SVCs in some observed supercells that are remarkably similar to the SVCs seen in numerical models, though there does appear to be a range of SVC characteristics and not all the sampled supercells appeared to have SVCs (Weiss et al. 2020). Though these RHIs provide promising evidence that the SVC does exist, the full 3D wind field cannot be accurately retrieved using a single radar, which prevents the examination of the  $\omega_s$  field. Using dual-Doppler wind syntheses can help circumvent this problem by retrieving the 3D wind field. Markowski et al. (2018) and Murdzek et al. (2020) each note features in their dual-Doppler wind syntheses that might resemble an SVC, but these features were not examined in depth, and in the case of Markowski et al. (2018), the feature was located on the edge of the dual-Doppler wind synthesis domain, making further inspection difficult.

To better understand the nature of SVCs in observed supercells, this article uses high-resolution dual-Doppler wind syntheses from three observed supercells, one of which has not been examined before using dual-Doppler and mobile mesonet platforms. Our guiding questions are as follows:

- Can SVCs be readily identified in observed supercells using dual-Doppler wind syntheses? Do all three supercells have SVCs?
- 2) Are the observed SVCs (if they exist) collocated with kinematic boundaries and thermodynamic gradients?
- 3) What is the vertical structure of the observed SVCs (if they exist)? Do they extend down close to the surface (i.e., height of mobile mesonet observations)?
- 4) Is there evidence that the SVC is augmented by baroclinic horizontal vorticity generation?

The goal is to use the knowledge gleaned from this study to guide future modeling endeavors that examine the SVC and its

<sup>&</sup>lt;sup>3</sup> It is worth emphasizing that the SVCs in these numerical simulations do *not* appear to be contributing vorticity to the tornado seed, whereas the vertical vorticity rivers mentioned earlier do contribute vorticity to the tornado seed.

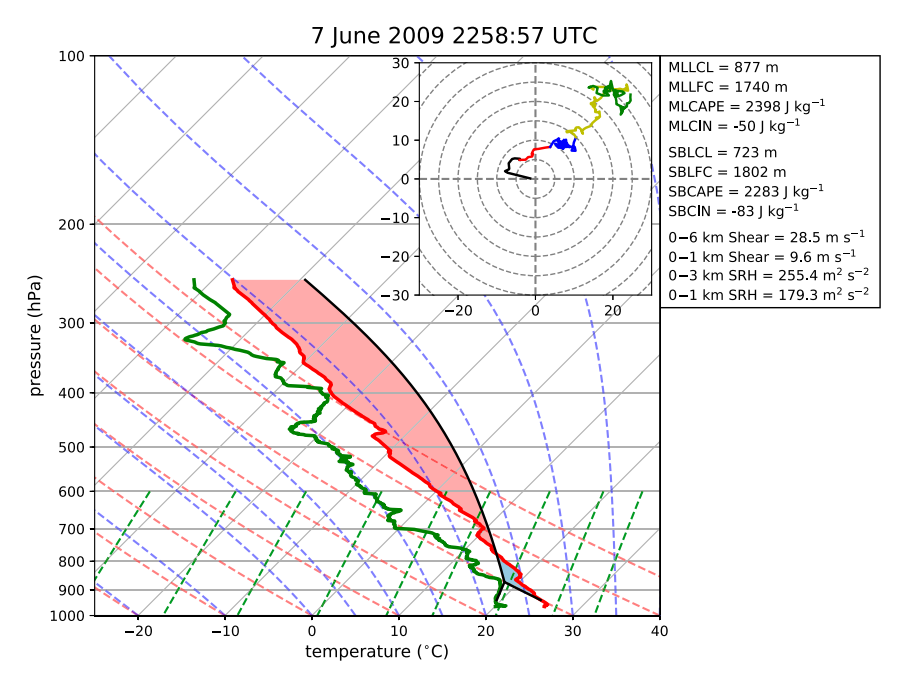


FIG. 1. Observed inflow sounding launched by VORTEX2 at 2258:57 UTC 7 Jun 2009 in northwestern Missouri. Solid red, green, and black lines on the skew *T*-log*p* diagram represent the temperature, dewpoint, and mixed-layer parcel temperature profiles, respectively, and the shaded red (blue) areas are proportional to the MLCAPE (MLCIN). The dashed red, blue, and green lines on the skew *T*-log*p* diagram represent the dry adiabats, pseudoadiabats, and constant water vapor mixing ratio lines, respectively. The different colored lines on the hodograph correspond to the winds between 0 and 0.5 km (black), 0.5 and 1 km (red), 1 and 3 km (blue), 3 and 6 km (yellow), and 6 and 9 km (green). For the sounding parameters, "ML" refers to a mixed-layer parcel (with the average characteristics of the lowest 50 hPa of the sounding) and "SB" refers to a surface-based parcel. The listed LFC, CAPE, and CIN are all computed using the virtual temperature correction (e.g., Doswell and Rasmussen 1994).

role in the intensification of the low-level mesocyclone, which is requisite for tornadogenesis.

# 2. Methodology

#### a. Case selection

The three cases examined herein come from the Second Verification of the Origins of Rotation in Tornadoes Experiment (VORTEX2; Wurman et al. 2012) and are listed in Table 1. The goal is to select cases with: (i) dual-Doppler on Wheels (DOW) coverage of the forward-flank region with a relatively short baseline (<12 km) and (ii) mobile mesonet observations in the forward flank during the time of dual-Doppler coverage. Satisfying these two criteria allows for the examination of the kinematics and near-surface thermodynamics of the SVC (if one can be identified) with relatively high spatial resolution. The three cases are from 7 June 2009 near Maysville, Missouri (hereafter the Maysville storm; discussed more in the next section); 11 June 2009 near La Junta, Colorado (hereafter the La Junta storm; Atkins et al. 2014); and 26 May 2010 near Prospect Valley, Colorado (hereafter the Prospect Valley storm; Tanamachi et al. 2013; Bowlan 2013; Murdzek et al. 2020). It is worth noting that it is not our objective to analyze every VORTEX2 intercept for evidence of an SVC and that the three cases we are examining may not be the only VORTEX2 cases that meet the two criteria outlined above, particularly when other mobile radars from the VORTEX2 armada are considered. Instead, this article is merely a first attempt to study observed SVCs (or the lack thereof) using a combination of dual-Doppler mobile radars and a mobile mesonet.

The classification of these storms as tornadic or nontornadic is not clear. VORTEX2 DOW7 crews observed a tornado-like vortex at 0112 UTC in the Maysville storm, which is also listed in the *Storm Data* publication as an EF0 tornado. The La Junta storm was visually unimpressive to VORTEX2 crews on the ground, yet *Storm Data* documents a brief, EF0 tornado associated with this storm at 0002 UTC. The Prospect Valley storm, as discussed in more detail in Tanamachi et al. (2013)

<sup>&</sup>lt;sup>4</sup>As discussed in the mobile mesonet report for the Maysville storm, there was some debate among VORTEX2 scientists as to whether this vortex should be considered a tornado. VORTEX2 reports for the Maysville storm can be found at <a href="http://catalog.eol.ucar.edu/cgi-bin/vortex2\_2009/report/index">http://catalog.eol.ucar.edu/cgi-bin/vortex2\_2009/report/index</a>.

TABLE 2. Parameters for the Barnes (1964) objective analysis and dual-Doppler wind synthesis. Grid spacing refers to both the vertical and horizontal grid spacing. All three cases use the same gridding and wind synthesis parameters.

Radar systems	DOW6 and DOW7		
Elevation angles	0.5°, 1.0°, 2.0°, 3.0°, 4.0°, 5.0°, 6.0°		
Coarsest data spacing (d)	0.35 km		
Distance from either DOW	20 km		
where data spacing $= d$			
Grid spacing $(\Delta x)$	0.125 km		
Barnes (1964) smoothing	$0.22\mathrm{km}^2$		
parameter $(\kappa_0)$			
Convergence parameter $(\gamma)$	0.3		
Minimum between-	$20^{\circ}$		
beam angle			

and Murdzek et al. (2020), contained a vortex that met a tornado threshold often used in mobile radar studies ( $40 \,\mathrm{m\,s}^{-1}$  inbound-outbound velocity difference between two gates  $\leq 2 \,\mathrm{km}$  apart; e.g., Alexander and Wurman 2008) around 2236 UTC. Given the fact that tens of experienced storm chasers with VORTEX2 did not note any features resembling a tornado in the La Junta

storm during the time period listed in Table 1, we are comfortable stating that the La Junta storm was nontornadic during the analysis time period, which is consistent with Parker (2014). The Maysville and Prospect Valley storms, on the other hand, will be regarded as weakly tornadic. At the very least, we can say with certainty that none of these three storms produced significant tornadoes during the time periods analyzed in this study.

## b. Overview of the 7 June 2009 Maysville, Missouri, storm

An overview of the Maysville storm will be briefly presented here because, to our knowledge, this storm has not been examined in the literature before beyond a brief examination of polarimetric features by Snyder et al. (2013). The environment in northeastern Kansas and northwestern Missouri was favorable for supercell development on 7 June 2009. A stationary front extended from Kansas into Nebraska and Iowa with near-surface dewpoints exceeding 20°C south of this front in northeastern Kansas and northwestern Missouri (Fig. 1). The combination of low-level moisture and lapse rates approaching the dry adiabatic lapse rate aloft resulted in mixed-layer convective available potential energy (CAPE) values exceeding 2300 J kg<sup>-1</sup>. The vertical wind profile was also favorable for supercell development, with 28.5 m s<sup>-1</sup> of 0–6-km shear (Fig. 1).

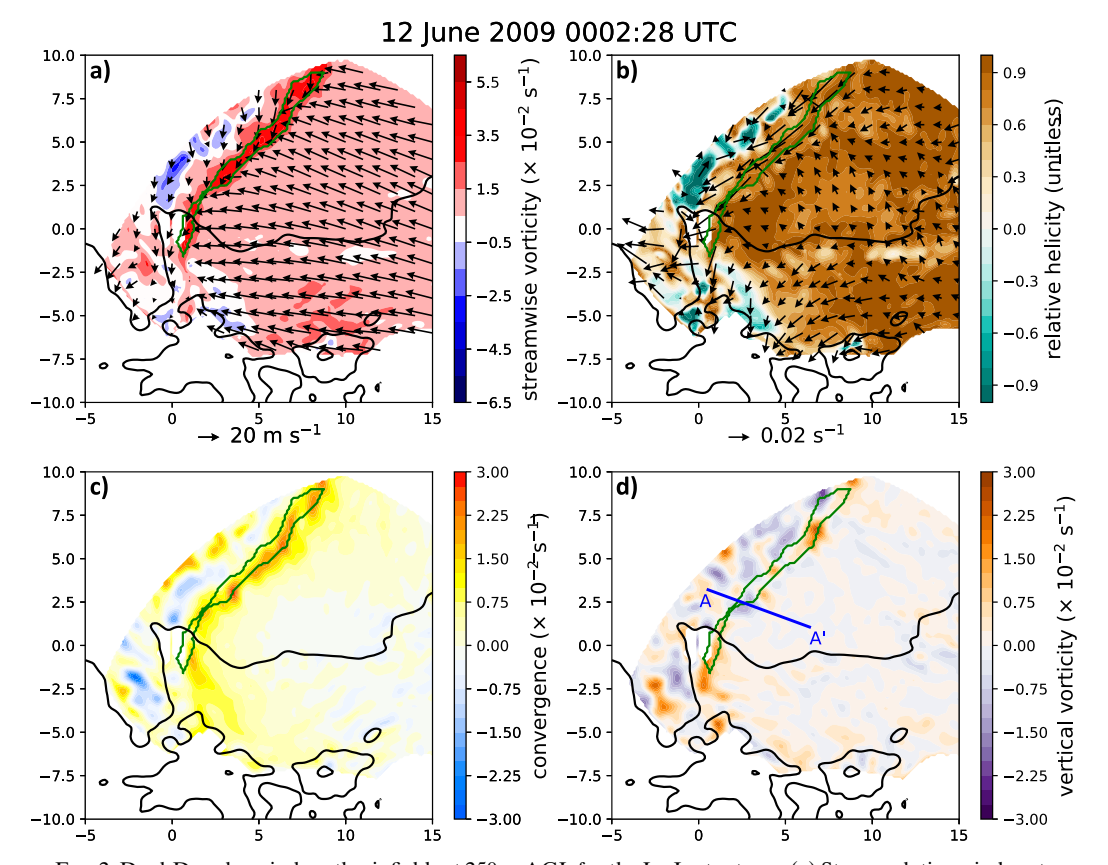


FIG. 2. Dual-Doppler wind synthesis fields at  $250\,\mathrm{m}$  AGL for the La Junta storm. (a) Storm-relative wind vectors and streamwise vorticity, (b) horizontal vorticity vectors and relative helicity, (c) horizontal convergence, and (d) vertical vorticity. In all four panels, the black contour is the 15-dBZ reflectivity outline at  $250\,\mathrm{m}$  AGL and the green contour is the objectively analyzed SVC at  $250\,\mathrm{m}$  AGL. The blue line in (d) denotes the location of the vertical cross section in Fig. 12. Axis labels are in km.

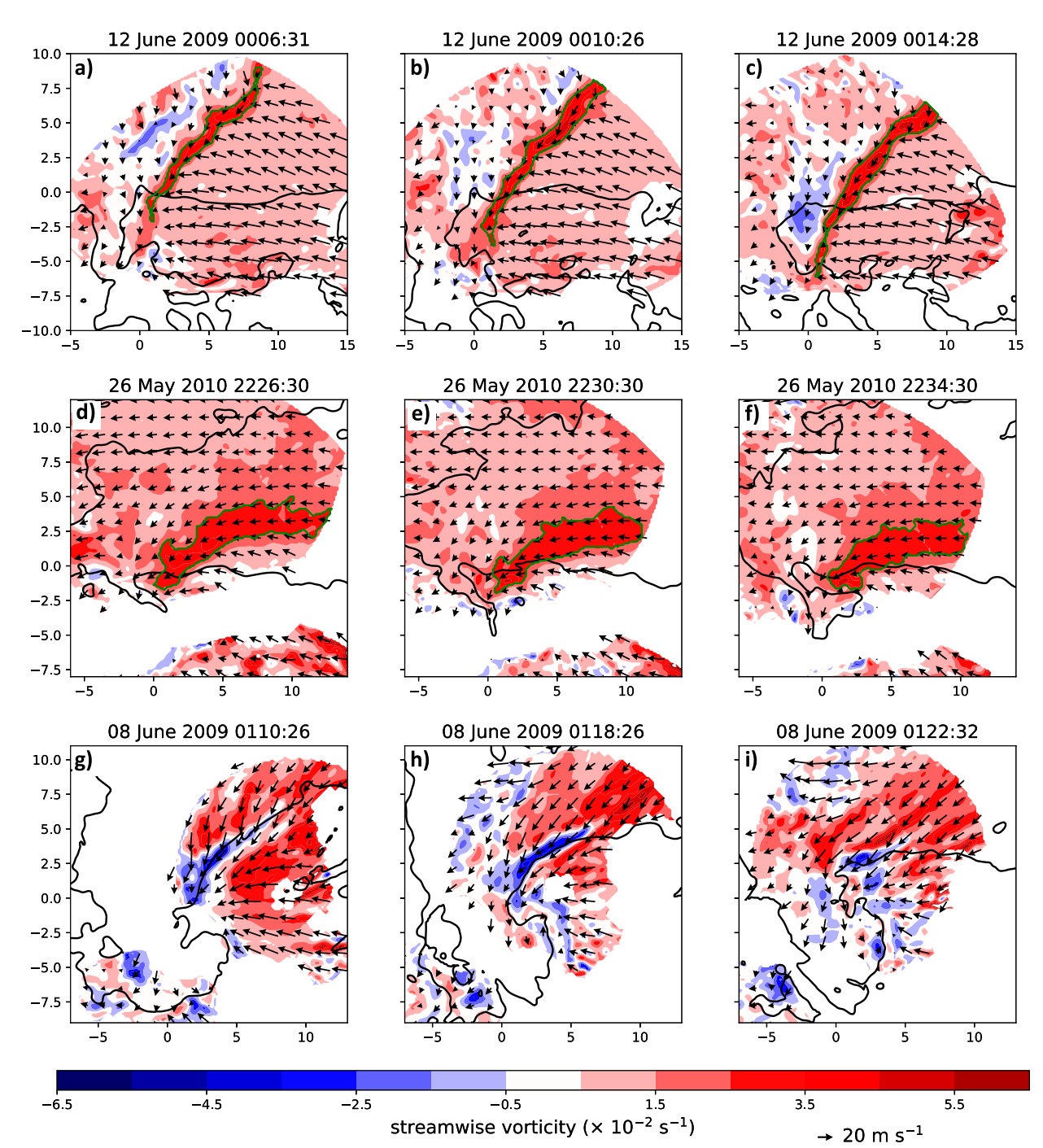


FIG. 3. Streamwise vorticity and horizontal storm-relative wind vectors at 250 m AGL for (a)–(c) the La Junta storm, (d)–(f) the Prospect Valley storm, and (g)–(i) the Maysville storm. The black contour denotes the 15-dBZ reflectivity outline at 250 m AGL and the green contour in (a)–(f) is the outline of the objectively analyzed SVC at 250 m AGL. Axis labels are in km and all times are in UTC.

The Maysville storm was initiated around 2100 UTC in northeastern Kansas along the aforementioned stationary front. Over the next 2 h, this storm moved to the northeast, and eventually started to propagate to the east and southeast after crossing the Missouri–Nebraska border at 2315 UTC. The storm maintained supercellular characteristics (e.g., a hook

echo) until  $\sim\!\!0300$  UTC, after which it started to weaken and move more to the northeast. The storm merged with other disorganized convection and became indistinguishable around 0500 UTC.

The Maysville storm was a prolific hail producer. *Storm Data* contains multiple reports of >3-in. hail (1 in. = 2.54 cm)

between 2330 and 0000 UTC, which is corroborated with VORTEX2 observations of baseball-sized hail during this time. During the period of interest (0054–0134 UTC, Table 1), *Storm Data* contains multiple hail reports associated with the Maysville storm. Two brief, weak tornadoes (each EF0) were also attributed to the Maysville storm in *Storm Data* at 0113 and 0127 UTC, and, as noted earlier, VORTEX2 crews noted the presence of a tornado-like vortex around 0112 UTC.

## c. DOW and mobile mesonet data processing

The DOW data are processed using the same methodology as Murdzek et al. (2020), except as noted below and in Table 2. A two-pass Barnes (1964) objective analysis scheme is used to grid the DOW data using a first-pass smoothing parameter of 0.22 km<sup>2</sup>, which, following Pauley and Wu (1990), is appropriate for radar data spacing ≤0.35 km. For the DOW elevation angles used, this corresponds to distances ≤20 km from either DOW (Table 2). For this reason, DOW data are only shown for grid points that are within 20 km of both DOWs. The objective analysis procedure suppresses high-frequency features, with 60% amplitude retained for features with a wavelength of 1 km and 90% amplitude retained for 1.7-km wavelengths. Given that the narrowest SVC from our three cases (the La Junta storm) has a width of 1-2 km, we are confident that the damping of the SVC from the objective analysis scheme is minimal. Following Koch et al. (1983), the horizontal and vertical grid spacings for the objective analysis are each 125 m, which matches the horizontal grid spacing<sup>5</sup> of the numerical simulations of an SVC performed by Schueth (2018). The dual-Doppler wind synthesis used to retrieve the 3D wind field is identical to Murdzek et al. (2020) with the exception that the downward extrapolation of winds during the vertical integration of the mass continuity equation is only allowed over a depth of 0.25 km instead of 1.4 km.

The processing of the mobile mesonet data also follows Murdzek et al. (2020), with deviations from the methodology of Murdzek et al. (2020) noted here. Thermodynamic data collected from stationary probes are discarded in the Maysville and La Junta storms owing to insufficient aspiration of the "J-tubes" used during VORTEX2 in 2009 (Waugh and Fredrickson 2010). After quality control and smoothing using a two-pass triangular filter, mobile mesonet analyses are created with a time-to-space conversion that uses a time window of 3 min. To explore the buoyancy gradients in the forward flank, mobile mesonet virtual potential temperature ( $\theta_v$ ), which is proportional to buoyancy if hydrometeor loading is ignored, is examined.

Dual-Doppler wind syntheses and mobile mesonet winds are also combined to estimate the streamwise horizontal vorticity beneath the dual-Doppler data horizon. The algorithm is as follows:

 Mobile mesonet observations within a 3-min time window centered on the dual-Doppler wind synthesis are time-tospace-converted to the dual-Doppler wind synthesis time.

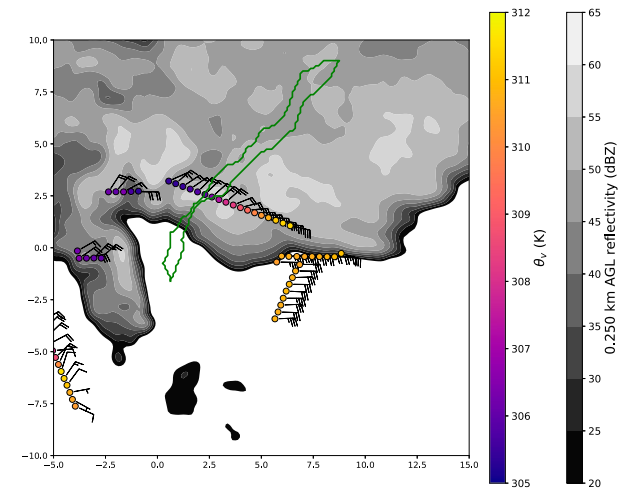


FIG. 4. Mobile mesonet observations in the La Junta storm at 0002:28 UTC. Station model colors represent  $\theta_v$  while the barbs denote storm-relative winds (full barb is  $5~{\rm m\,s^{-1}}$  and a half barb is  $2.5~{\rm m\,s^{-1}}$ ). The 250 m AGL dual-Doppler reflectivity field (gray shading) and objectively analyzed SVC at 250 m AGL (green contour) are also included. Axis labels are in km.

- 2) Each mobile mesonet observation is paired with the closest dual-Doppler wind synthesis grid point at the lowest vertical level with widespread dual-Doppler data ( $z=125\,\mathrm{m}$  for the Maysville and Prospect Valley storms and  $z=250\,\mathrm{m}$  for the La Junta storm). The horizontal distance between the mobile mesonet observation and dual-Doppler wind synthesis grid point must be less than the dual-Doppler wind synthesis grid spacing (125 m), otherwise the mobile mesonet observation is ignored.
- 3) Compute the average vertical wind shear (horizontal velocity differential) using the mobile mesonet wind [at 2 m above ground level (AGL)] and dual-Doppler wind synthesis horizontal wind (at 125 or 250 m AGL).
- 4) Compute the horizontal vertical velocity gradient using the dual-Doppler wind synthesis vertical velocities (at 125 or 250 m AGL). Divide these gradients by 2 to get an estimate of the horizontal vertical velocity gradient halfway between the surface and dual-Doppler data horizon (this assumes that the vertical velocity is 0 at the surface).<sup>6</sup>
- 5) Compute the average horizontal vorticity from the average vertical wind shear and estimated vertical velocity gradient, then partition the horizontal vorticity into streamwise and crosswise components using the mean horizontal stormrelative wind vector (computed as the average of the mobile mesonet and dual-Doppler wind synthesis winds).

<sup>&</sup>lt;sup>5</sup>Even though the grid spacing in the dual-Doppler wind synthesis matches the simulations performed by Schueth (2018), the resolutions are not necessarily the same, owing in part to the smoothing that is implicit to the radar objective analysis scheme.

 $<sup>^6</sup>$  This method of estimating the horizontal gradient of vertical velocity is admittedly crude, but it ultimately has a minimal impact on horizontal vorticity magnitude. Root-mean-square differences between horizontal vorticity beneath the dual-Doppler data horizon computed with and without the horizontal gradient of the vertical velocity are  $<0.002\,\mathrm{s}^{-1}$ , which is an order of magnitude less than the values in Figs. 14 and 15

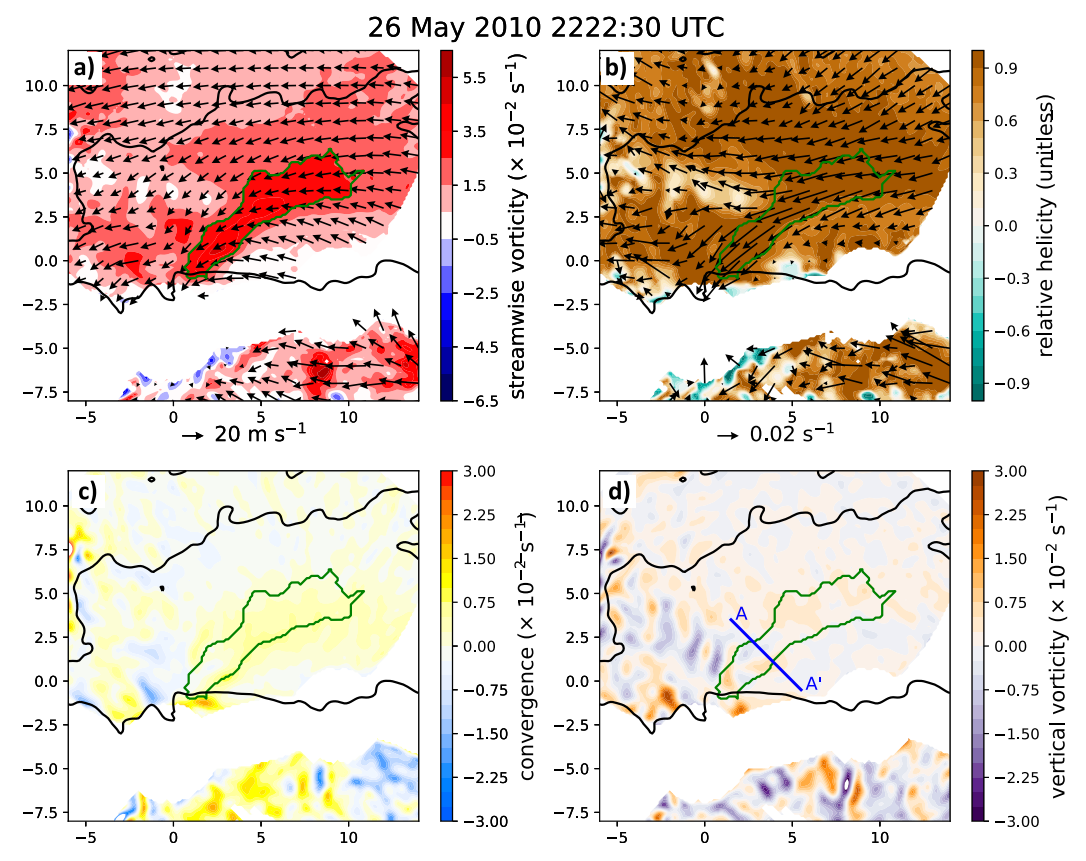


FIG. 5. As in Fig. 2, but for the Prospect Valley storm at 2222:30 UTC.

It is important to note that changes in the elevation of the mobile mesonet probes owing to topography are not accounted for in this algorithm. Such changes in elevation would impact the magnitude, but not the direction, of the layer-averaged horizontal vorticity.

# d. Identification of the SVC

An objective definition of the SVC is needed in order to proceed with analyzing it. The approach used here is based on Schueth (2018), with some modifications. For each vertical level in the dual-Doppler wind synthesis, regions with  $\omega_s \ge 0.025 \, \mathrm{s}^{-1}$  are identified.<sup>7</sup> After using a binary closing scheme to fill any gaps (similar to Schueth 2018), the largest region with  $\omega_s \ge 0.025 \, \mathrm{s}^{-1}$  is selected as the SVC. The shape and storm-relative location of the SVC outline on each vertical level between 125 and 500 m is then subjectively examined to make sure the SVC has vertical continuity (if the shape and/or location of the SVC outline varies greatly with height, the feature is not identified as an SVC). Based on the simulation of Schueth (2018), the maximum  $\omega_s$  values within the SVC occur between 250 and 500 m AGL, so examining the 125–500-m

vertical layer gives the best chance for finding an SVC. After checking for vertical continuity, temporal continuity is subjectively checked by ensuring that the SVC has a similar storm-relative position in consecutive time steps and the shape of the SVC does not change rapidly with time. The  $\omega_s$  threshold of  $0.025 \, \mathrm{s}^{-1}$  for the SVC is fairly arbitrary and is chosen because it is similar to the value of  $0.03 \, \mathrm{s}^{-1}$  used by Schueth (2018) and captures what one might subjectively consider to be the SVC in the storms considered in this article. It is likely that this threshold is not appropriate for all supercells and that it changes with grid resolution.

# 3. Observations

#### a. The La Junta storm

The La Junta storm exhibits a feature that meets our definition of an SVC (green contour in Fig. 2). The SVC in the La Junta storm is a narrow zone of enhanced  $\omega_s$  with values in some areas that are more than twice as large as the  $\omega_s$  values in the rest of the forward flank (which also contains appreciable  $\omega_s$ , Fig. 2a). The SVC makes a rather large angle with the 15-dBZ reflectivity contour (black line in Fig. 2) and maintains a similar storm-relative position and appearance with time (Figs. 3a-c). Although only four times are presented here for brevity, the SVC in the La Junta storm can be seen from 0000 to 0022 UTC at 250, 375, and 500 m AGL (not shown).

 $<sup>^{7}</sup>$  The value of  $\omega_{s}$  is computed using Eq. (1) with the 3D wind vector from the dual-Doppler wind synthesis and the average storm motion over the analysis period.

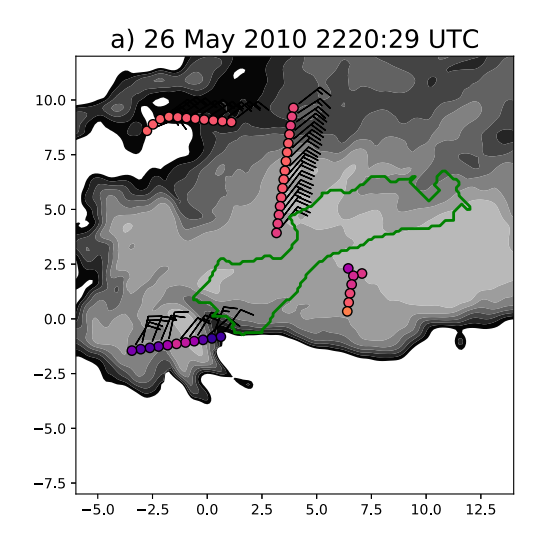
After 0022 UTC, the SVC becomes hard to identify owing to its proximity to the eastern edge of the dual-Doppler wind synthesis domain.

The La Junta SVC will be examined in detail at 0002:28 UTC owing to the fact that there is also a mobile mesonet transect through the SVC at this time. The kinematic characteristics of the SVC discussed here can be seen at all times that the SVC can be identified. Horizontal vorticity within the SVC is much larger compared to the rest of the forward flank, whereas the relative helicity (defined as the ratio of  $\omega_s$  to the magnitude of the 3D vorticity vector) within the SVC is similar to the rest of the forward flank (Fig. 2b). This suggests that the enhanced  $\omega_s$ within the SVC is likely the result of larger vorticity values rather than a more favorable orientation between the velocity and vorticity vectors. Both the horizontal wind vectors and horizontal convergence (hereafter simply "convergence") fields indicate that the SVC is collocated with a kinematic boundary (similar to the left-flank convergence boundary of Beck and Weiss 2013), with the strongest convergence on the inflow (eastern) side of the SVC (Figs. 2a,c). In terms of vertical vorticity, there are some patches of enhanced vertical vorticity (both positive and negative) along the SVC, but in general there is no tendency for the SVC to favor positive or negative vertical vorticity (Fig. 2d). Some of these patches appear to move toward the hook echo with time (not shown) in a manner reminiscent of the vertical vorticity patches in the vertical vorticity sheet simulated by Orf et al. (2017). It is worth noting that the vertical vorticity field on the outflow (western) side of the SVC has a visual appearance that is much more turbulent compared to the more laminar modified inflow to the east of the SVC (Fig. 2d). This matches the hypothesis of Brandes et al. (1988) that the rear flank of a supercell tends to be more turbulent than the forward flank and is similar to high-resolution numerical simulations of supercells (e.g., Fig. 1 from Markowski and Bryan 2016). A mobile mesonet transect through the SVC at 0002:28 UTC shows confluent winds ~1 km ahead of the SVC that are collocated with a strong buoyancy gradient (Fig. 4). The presence of the SVC on the cool side of this near-surface boundary matches the numerical simulation of Orf et al. (2017).

# b. The Prospect Valley storm

Dual-Doppler wind syntheses of the Prospect Valley storm also display a feature that meets our definition of an SVC (Fig. 5). Unlike the La Junta storm, the SVC in the Prospect Valley storm is much wider (~2.5 km) and makes a smaller angle with the 15-dBZ reflectivity contour (Fig. 5). The SVC in the Prospect Valley storm has a similar appearance and storm-relative position in all four times presented here (Figs. 3d–f and 5a) and can also be seen at each vertical level between 125 and 500 m AGL for each time between 2218 and 2236 UTC. After 2236 UTC, the SVC appears less organized and is also more difficult to identify given its proximity to the eastern edge of the dual-Doppler wind synthesis domain.

In many ways, the Prospect Valley SVC is similar to the La Junta SVC. Horizontal vorticity is strongest within the SVC of the Prospect Valley storm, and relative helicity is slightly larger



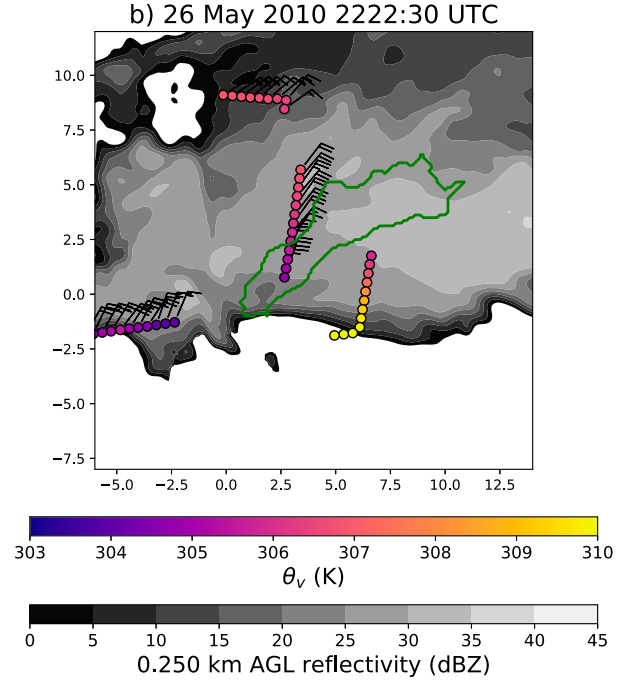


FIG. 6. As in Fig. 4, but for the Prospect Valley storm at (a) 2220:29 and (b) 2222:30 UTC.

within the SVC compared to the inflow to the southeast (Fig. 5b). Convergence, albeit weaker than the La Junta SVC, can be subtly seen on the inflow (southeastern) side of the SVC (Fig. 5c). This convergence is stronger at 125 m AGL (not shown) and is collocated with confluence in the horizontal wind vectors (Fig. 5a). There is a tendency for the Prospect Valley SVC to favor slightly positive vertical vorticity (though these values are no larger than other portions of the forward flank), and like the La Junta SVC, there is some tendency for the vertical vorticity field to be more turbulent on the outflow (northwestern) side of the SVC (Fig. 5d). Mobile mesonet transects near the SVC suggest that the SVC is collocated with a near-surface buoyancy minimum with a relatively strong

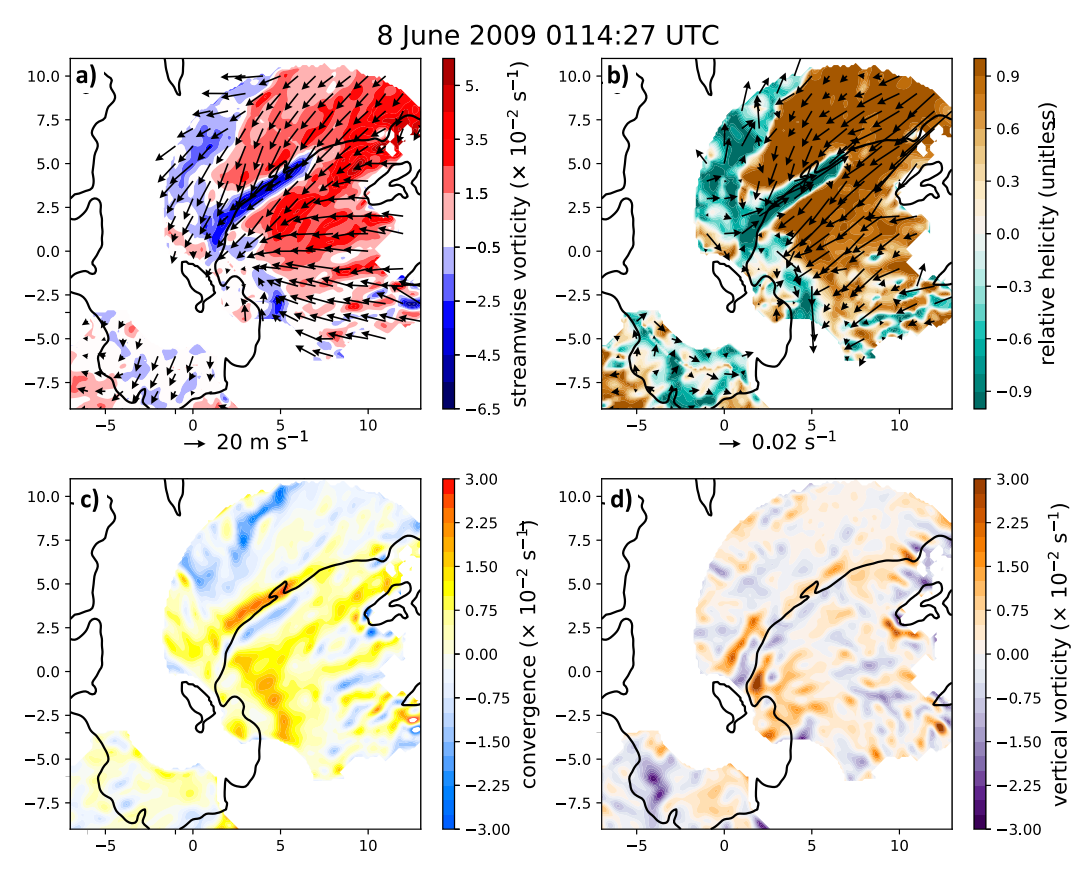


FIG. 7. As in Fig. 2, but for the Maysville storm at 0114:27 UTC.

buoyancy gradient on the inflow side (compared to the outflow side of the SVC, Fig. 6).

# c. The Maysville storm

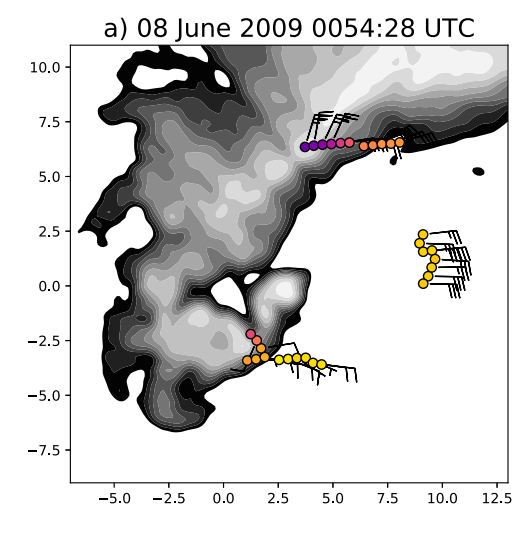
Unlike the La Junta and Prospect Valley storms, the Maysville storm does not have a feature that can be clearly identified as an SVC. Plots of  $\omega_s$  at 250 m AGL at four different times show broad regions with appreciably  $\omega_s$  both in the inflow to the east of the hook echo and within the forward flank north of the 15-dBZ reflectivity contour (Figs. 3g-i and 7a). Ribbonlike  $\omega_s$  maxima can be seen at some times [e.g., from (5.0, 1.5) to (10.0, 5.0) in Fig. 7a], but such maxima have poor temporal continuity and the  $\omega_s$  values within these maxima are not that much greater than the rest of the inflow and forward flank. As a result, we conclude that based on this dual-Doppler dataset, the Maysville storm does not appear to have an SVC (or at least, not a well-defined SVC).

Other aspects of the Maysville storm differ from the La Junta and Prospect Valley storms. Horizontal vorticity is large across much of the inflow and southern forward-flank regions and is not confined to a narrow region like in the other two storms (Fig. 7b). The convergence and vertical vorticity fields are also rather heterogeneous throughout the entire inflow region and southern portion of the forward flank (Figs. 7c,d). One of the only aspects of the Maysville storm that is similar to the La Junta and Prospect Valley storms is the presence of

relative helicity values near unity throughout most of the forward flank and inflow regions. Another similarity between the Maysville storm and the other two storms is the prominent forward-flank convergence boundary (FFCB; Beck and Weiss 2013) that can be seen along the 15-dBZ reflectivity contour (Fig. 7c). Although the storm-relative position of this boundary differs from the other two storms, it also features confluent mobile mesonet winds and a strong buoyancy gradient (Fig. 8), similar to the boundaries in the La Junta and Prospect Valley storms.

Interestingly, although it lacks a well-defined SVC, the Maysville storm exhibits a ribbon of antistreamwise vorticity along a portion of the 15-dBZ reflectivity contour near the hook echo [e.g., from (2.5, 2.0) to (7.0, 5.0) in Fig. 7a]. This antistreamwise vorticity ribbon (hereafter AVR) deviates from supercell conceptual models, so it is worth examining this feature with more scrutiny to determine if it is an artifact. We start by seeing if the AVR can be deduced from plan position indicator (PPI) displays from DOW6 and DOW7. The 1.0° elevation angle PPIs for both DOW6 and DOW7 show a slice of weakly negative radial velocities within a much larger region of stronger negative radial velocities where the AVR is observed in the dual-Doppler wind syntheses (Figs. 9b and 10b). The AVR can be deduced from these weakly negative radial velocities in two ways. First, the radial velocities within the AVR become more negative with height (unlike the surrounding

304



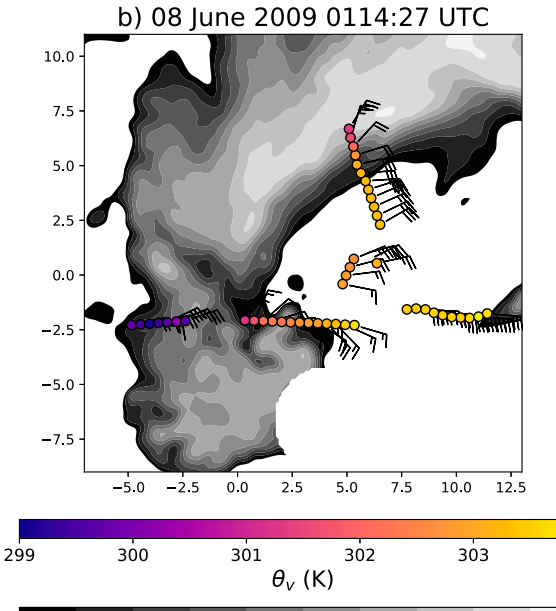


Fig. 8. As in Fig. 4, but for the Maysville storm at (a) 0054:28 and (b) 0114:27 UTC.

30

0.250 km AGL DOW6 reflectivity (dBZ)

35

region, where the radial velocities become less negative with height), which results in a horizontal vorticity vector oriented toward the east, opposite the flow in this region (see Fig. 7a). Second, the radial velocity field suggests the presence of a transverse circulation with convergence (likely associated with upward motion by mass continuity) northwest of the AVR and divergence (likely associated with downward motion) southeast of the AVR. This transverse circulation would result in a northeastward-pointing vorticity vector, which also opposes the flow. The fact that the AVR can be seen in single-Doppler scans suggests that it is not an artifact of the dual-Doppler wind synthesis procedure, nor is it the result of one of the radars malfunctioning (unless both were malfunctioning simultaneously).

So are the weakly negative radial velocities observed by DOW6 and DOW7 representative of the airflow in that region? The odd appearance of the weakly negative radial velocities and its location along a reflectivity gradient suggests that it may be an artifact. The normalized coherent power and spectrum width in this region, however, are not that much different from the surrounding regions<sup>8</sup> (Figs. 9c,d and 10c,d). This observation, coupled with the fact that the reflectivity values in the vicinity of the AVR weaken with height (i.e., the 15-dBZ reflectivity contour slopes to the northwest with height) suggests that the weakly negative velocities are likely not the result of vertical sidelobes. Furthermore, the fact that weakly negative velocities are present in both DOWs in the same storm-relative region for ~20 min despite different viewing perspectives further suggests that the AVR may not be an artifact. Another hypothesis is that the weakly negative radial velocities are the result of large hail that is moving slower than the rest of the flow, owing to its large inertia (e.g., section 3 from Wang et al. 2019). As discussed in section 2b, multiple reports of hail associated with the Maysville storm occurred during the analysis period, and polarimetric radar observations from UMass X-Pol at 0120 UTC show reduced differential reflectivity and correlation coefficient values at altitudes just above the AVR (not shown), which is suggestive of hail (e.g., Kumjian 2013). The lack of large reflectivity values in the DOW data near the AVR may counter the claim that hail was occurring in this part of the storm (Figs. 9a and 10a), but sparse populations of large hail may not be associated with large reflectivity, especially at X band owing to resonance effects (Kumjian et al. 2018). Thus, hail was likely present near the AVR, though we are hesitant to attribute such a large reduction in the absolute value of the radial velocity compared to the surrounding regions (at least 10 m s<sup>-1</sup>, Fig. 9b) solely to the presence of hail, especially given the mobile mesonet observations presented in the next paragraph.

In an effort to get an independent measurement of the winds near the AVR without the potential influence of hail, mobile mesonet data are examined. Figure 11 shows the mobile mesonet wind component that points away from DOW6 for a probe that transects the forward-flank reflectivity gradient around 0114:27 UTC. Interestingly, the pattern of the mobile mesonet winds projected onto the vector that points radially away from DOW6 is similar to the gridded DOW6 radial velocities. Furthermore, the mobile mesonet winds are diffluent where radial divergence is observed in DOW6 near (6.0, 4.0) and confluent where radial convergence is observed in DOW6 near (5.5, 4.5). This matches the transverse circulation pattern noted above and suggests that the wind field observed by the DOWs is

<sup>&</sup>lt;sup>8</sup>The line of reduced normalized coherent power and increased spectrum width immediately north of the AVR is likely a signal of the FFCB. Similar signatures are observed along boundaries in the La Junta and Prospect Valley storms and are expected given the large wind shifts associated with these boundaries.

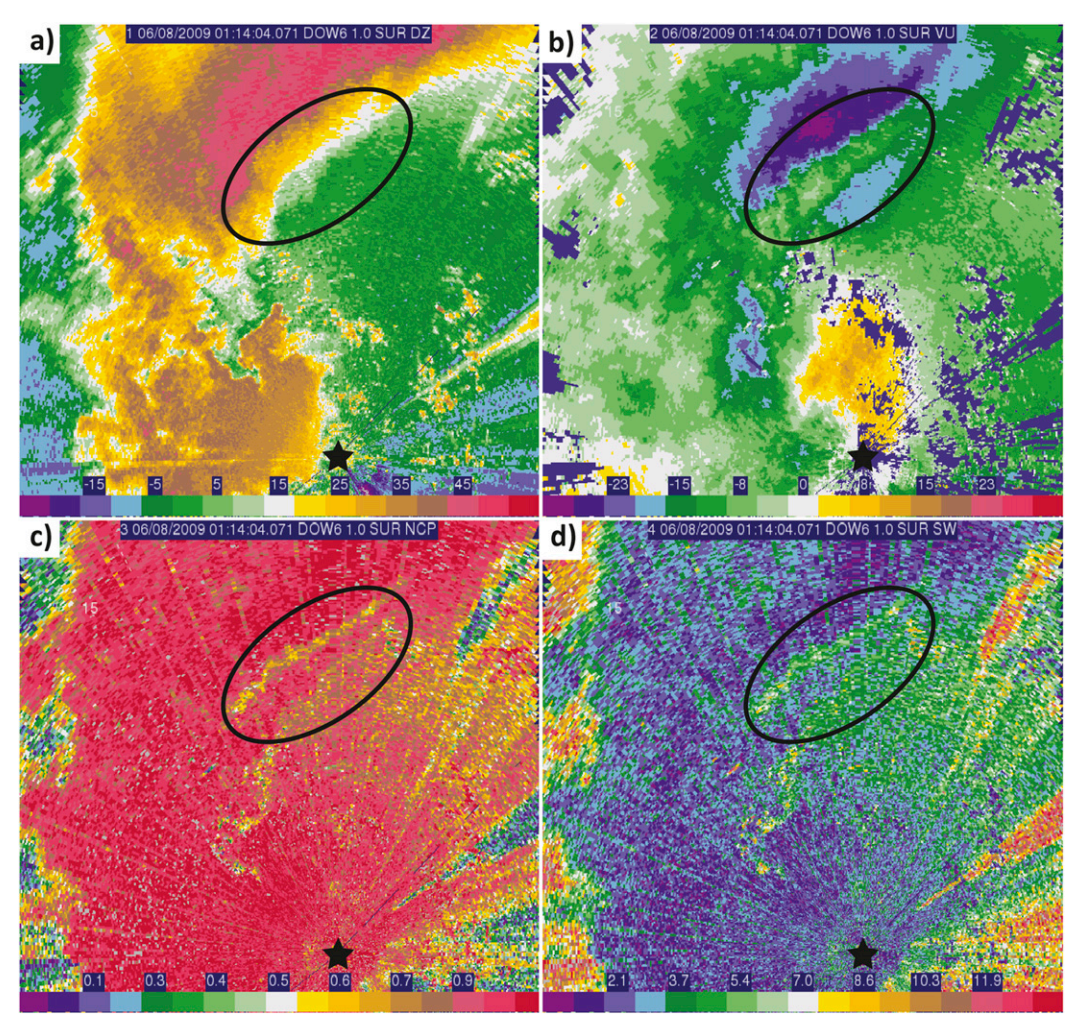


FIG. 9. DOW6  $1.0^{\circ}$  PPI for the Maysville storm at 0114:04 UTC. (a) Uncalibrated reflectivity (dBZ), (b) radial velocity (m s<sup>-1</sup>), (c) normalized coherent power (unitless), and (d) spectrum width (m s<sup>-1</sup>). The black oval denotes the zone of weakly negative radial velocities discussed in the text and the black star is the location of DOW6.

representative of the flow within the Maysville storm. With no clear reason to remove the weakly negative radial velocity slice that resulted in the AVR in the dual-Doppler wind syntheses, we can only cautiously suggest that the AVR might be a flow feature of the Maysville storm, though its strength may be enhanced by the presence of hail. It is worth noting that a feature similar to the AVR was observed by Beck et al. (2006) in the 29 May 2001 Kress, TX, supercell (see their Fig. 14), but the antistreamwise vorticity signature in Beck et al. (2006) was only visible above 0.5 km AGL, whereas the Maysville AVR can be clearly seen at lower levels. A feature similar to the AVR has also been observed in a high-resolution simulation of a tornadic supercell prior to tornadogenesis, but this feature is located to the rear of the coldest air within the cold pool (L. Orf 2020, personal communication), unlike the AVR presented here, which had a more forward position. Finally, it is also worth noting that even if the AVR is found to be an artifact and the weakly negative radial velocities are removed, this would

not change the primary conclusion of this subsection that the Maysville storm lacks a well-defined SVC.

## 4. Discussion

The third question posed in section 1 involves the vertical structure of the SVC and whether there is evidence of the SVC near the surface. Vertical cross sections perpendicular to the primary axis of the SVCs of the La Junta and Prospect Valley storms both show regions of enhanced  $\omega_s$  that slope toward the rear of the supercell with height and have local maxima in  $\omega_s$  aloft in what resembles the head of a density current ( $x=0.8\,\mathrm{km}$  in Fig. 12 and  $x=0.5\,\mathrm{km}$  in Fig. 13), though we have not evaluated whether the outflow in this region is best characterized as a density current [based on the simulations of Beck and Weiss (2013), left-flank outflow may not be expected to be characterized as a density current]. These cross sections through the SVCs are similar in appearance to synthetic RHIs through an SVC in a supercell simulated by Schueth (2018)

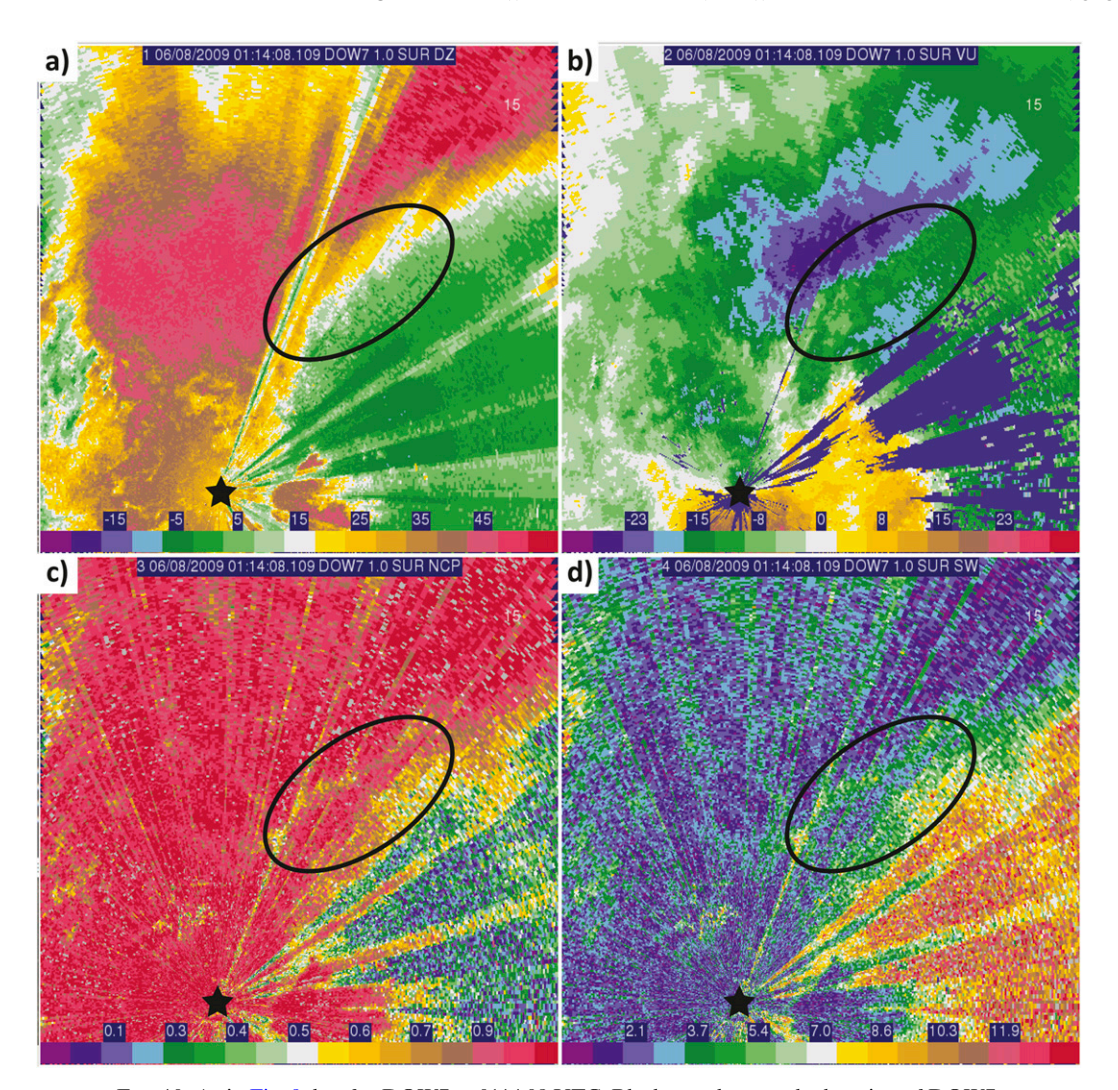


FIG. 10. As in Fig. 9, but for DOW7 at 0114:08 UTC. Black star denotes the location of DOW7.

(their Figs. 3.7–3.15). The objectively analyzed SVCs in both of our cases, as indicated by the black contour, extend down to the lowest vertical level with dual-Doppler wind synthesis data. Furthermore, estimates of the 2-250-m average streamwise horizontal vorticity in the La Junta storm and 2–125-m average streamwise horizontal vorticity in the Prospect Valley storm show clear maxima on the inflow side of the 250-m SVC contour with values close to or exceeding the SVC  $\omega_s$  threshold of  $0.025\,\mathrm{s}^{-1}$  (Figs. 14 and 15 ). Thus, these observations suggest that the SVC extends down close to the surface with values of  $\omega_s$  that are comparable to those found farther aloft, though it is worth mentioning that the implicit smoothing of the radar gridding algorithm may be inflating  $\omega_s$  values at lower levels within the dual-Doppler wind syntheses. In the Prospect Valley case, the largest  $\omega_s$  values are actually found at the lowest levels of the dual-Doppler wind synthesis (≤250 m) below the density-current-like head mentioned above, and may be even stronger below the dual-Doppler data horizon (Fig. 15). This is in contrast with the SVCs simulated by Schueth (2018), which are strongest farther aloft within the head. Collectively, these

results suggest that the vertical structure of simulated and observed SVCs are generally similar, though there are some discrepancies regarding the location of the maximum  $\omega_s$ .

Another question posed in the introduction is whether there is evidence of baroclinic generation of  $\omega_s$  within the SVC. The near-surface buoyancy gradients located slightly ahead (in a storm-relative sense) of the SVC observed by the mobile mesonet in the La Junta and Prospect Valley storms (Figs. 4 and 6) provide compelling evidence that  $\omega_s$  within the SVC is likely augmented by baroclinic generation. The fact that the horizontal vorticity vectors are much longer within the SVC compared to the surrounding regions also supports this claim (Figs. 2b and 5b). In the inviscid, Boussinesq limit,  $\omega_s$  can be generated through crosswise-to-streamwise conversion, tilting and stretching, and baroclinity (e.g., Adlerman et al. 1999). If the enhanced  $\omega_s$  within the SVC was purely the result of crosswise-to-streamwise conversion (i.e., the "riverbend effect"), such a drastic change in the magnitude of the vorticity vectors within the SVC would not be expected because only the orientation of the vorticity vectors would change, not their

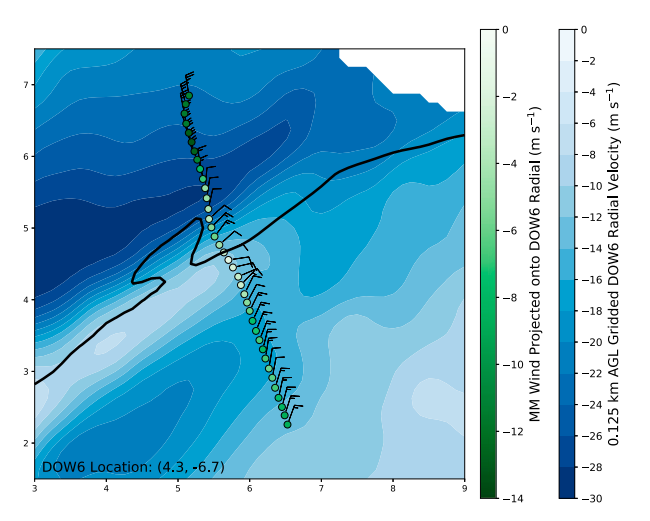


FIG. 11. Objectively analyzed DOW6 radial velocities at 125 m AGL (blue shading) and mobile mesonet station models at 0114:27 UTC for the Maysville storm. Station model shading indicates the projection of the mobile mesonet ground-relative wind onto the vector pointing from DOW6 to the mobile mesonet probe. Wind barbs denote the mobile mesonet-observed ground-relative winds with a full (half) barb denoting 5.0 (2.5) m s<sup>-1</sup>. Black contour is the 15-dBZ reflectivity contour at 250 m AGL and all axis labels are in km.

magnitude. Furthermore, if crosswise-to-streamwise conversion were responsible for the enhanced  $\omega_s$  within the SVC, relative helicity would be expected to greatly increase within the SVC compared to the surrounding areas, which is also not the case (Figs. 2b and 5b). In addition to baroclinic generation, it is also possible that horizontal stretching of  $\omega_s$  may be increasing the vorticity vector magnitude within the SVC, but there is little indication of the horizontal winds accelerating in the direction of the vorticity vectors in either the La Junta or Prospect Valley storms (Figs. 2a, 5a, and 3a-f). This leaves baroclinic generation of horizontal vorticity and processes not accounted for in the inviscid, Boussinesq limit, such as frictional effects (e.g., Schenkman et al. 2014), as the likely culprits as to why  $\omega_s$  within the SVC is so much stronger than the surrounding areas. In short, there is evidence that the SVCs of the La Junta and Prospect Valley storms are augmented by baroclinic vorticity generation, though we cannot rule out the possibility that frictional generation of  $\omega_s$  may also be contributing to the SVC.

Returning to the first question in the introduction about the ubiquity of SVCs, the results presented herein suggest that not all supercells contain SVCs, similar to the preliminary results of the 2019 TORUS field campaign. The fact that the Maysville storm, which was weakly tornadic, did not have a well-defined SVC while the other two storms, one of which was nontornadic, did have well-defined SVCs suggests that the presence of an SVC is not necessary for tornadogenesis and that the presence of an SVC does not guarantee tornadogenesis will occur. In fact, the presence of an SVC may be a "double-edged sword" in promoting tornadogenesis. A strong SVC may result in a stronger low-level mesocyclone with larger dynamic pressure

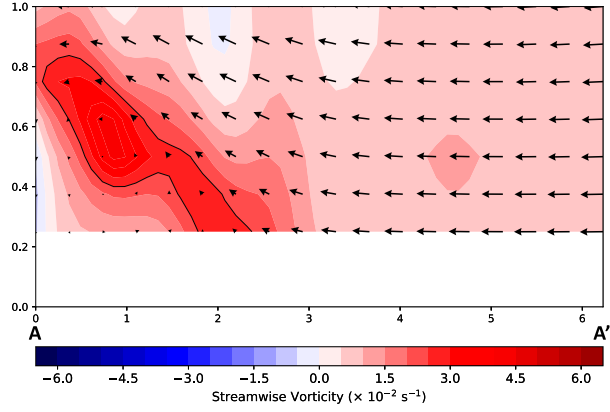


FIG. 12. Vertical cross section through the SVC of the La Junta storm at 0002:28 UTC (see Fig. 2 for location). Streamwise vorticity (color shading), wind vectors, and 0.025-s<sup>-1</sup> streamwise vorticity contour (black line) are plotted. Axis labels are in km.

falls that results in a stronger upward-directed VPPGF (e.g., Orf et al. 2018), but such a strong SVC would likely be coupled with larger buoyancy deficits within the forward-flank cold pool, as suggested by Schueth and Weiss (2020). Previous observational studies have shown a robust trend that the likelihood of tornadogenesis decreases with increasing outflow negative buoyancy (e.g., Markowski et al. 2002; Shabbott and Markowski 2006; Grzych et al. 2007). Therefore, a balance perhaps needs to be struck between a cold pool that is strong enough to produce a strong SVC (and by extension, a stronger low-level mesocyclone), but not so strong that excessive negative buoyancy greatly inhibits vertical vorticity stretching within the circulation-rich outflow.

The lack of an SVC also does not appear to imply that there are not large  $\omega_s$  values within a storm, nor does it seem to imply the absence of baroclinic generation of  $\omega_s$ . In the Maysville storm, broad areas with  $\omega_s \ge 0.015 \,\mathrm{s}^{-1}$  are seen throughout the inflow and forward-flank regions (Figs. 7a and 3g-i). The presence of a near-surface buoyancy gradient orthogonal to the 15-dBZ reflectivity contour suggests that some baroclinic generation of horizontal vorticity may have been occurring (Fig. 8). It is possible that the structure of certain storms, such as the Maysville storm, are not conducive to organizing  $\omega_s$  into coherent "tubes" that are characteristic of an SVC. It could be that the inflow of the Maysville storm was too turbulent (as seen in the vertical vorticity field, Fig. 7d) for a well-defined SVC to form. The more chaotic nature of the flow within the Maysville storm may be the result of the mesoscale environment in which it formed, interaction with other convective cells in the area, or differences in surface roughness between northwestern Missouri (where the Maysville is located) and eastern Colorado (where the La Junta and Prospect Valley are). The mesoscale environment may also play a role in the organization of  $\omega_s$  into an SVC; in the La Junta storm, for instance, outflow from a supercell to the north may have enhanced the northerly flow behind the SVC (as mentioned in Atkins et al. 2014), resulting in a more compact SVC.

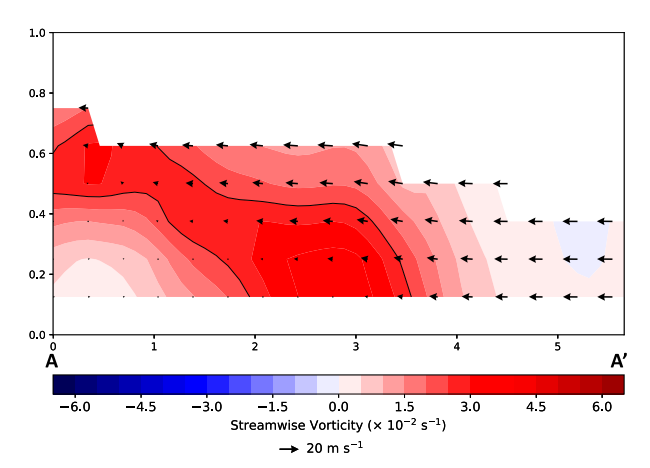


FIG. 13. As in Fig. 12, but for the Prospect Valley storm at 2222:30 UTC.

#### 5. Conclusions

Dual-Doppler wind syntheses and mobile mesonet observations from three VORTEX2 supercells, one of which (the Maysville storm) has not been previously examined using these platforms, are examined to answer four questions related to the SVC, a feature seen in recent high-resolution numerical simulations. The answers to these questions are as follows:

- 1) High-resolution (125-m grid spacing) dual-Doppler wind syntheses are capable of identifying SVCs that are akin to those in numerical simulations. Similar to preliminary TORUS observations (Weiss et al. 2020), SVCs do not appear to be a ubiquitous feature in all supercells (only two of the three supercells examined had an SVC) and the lack of an SVC does not appear to preclude the formation of weak tornadoes. Furthermore, the presence of an SVC does not guarantee that a tornado will form.
- 2) The SVCs in the La Junta and Prospect Valley storms formed along the outflow side of boundaries within the forward flank that were observed in both the dual-Doppler wind synthesis and mobile mesonet data. Both boundaries appeared to separate colder and more turbulent outflow from warmer and more laminar modified inflow. These observations generally match the characteristics of SVCs in simulated supercells.
- 3) Both of the observed SVCs have a vertical structure similar to SVCs in simulated supercells (i.e., reminiscent of a density current with an  $\omega_s$  local maxima in the head), though the strongest  $\omega_s$  values in the Prospect Valley SVC are found at lower levels compared to a simulated SVC.
- 4) The presence of near-surface buoyancy gradients and larger vorticity vectors in the vicinity of the two observed SVCs suggests that streamwise vorticity within the observed SVCs is augmented by baroclinic generation.

In addition to the results listed above, considerable variability in SVC width and position was observed between the La Junta and Prospect Valley storms.

The Maysville storm exhibited an antistreamwise vorticity ribbon (AVR) along the southern border of the forward flank.

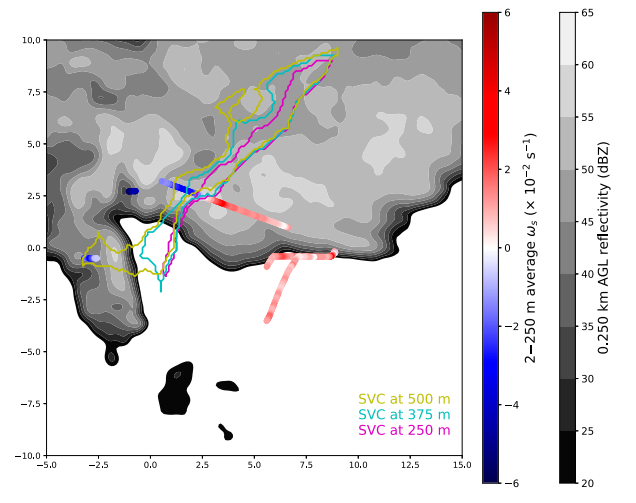


FIG. 14. SVC vertical structure in the La Junta storm at 0002:28 UTC. The blue and red lines denote the average streamwise horizontal vorticity in the 2–250-m layer computed using mobile mesonet and dual-Doppler wind synthesis winds (see section 2c for details). Yellow, cyan, and purple lines show the outline of the objectively analyzed SVC at 500, 375, and 250 m AGL, respectively. Gray shading shows the dual-Doppler reflectivity at 250 m AGL. Axis labels are in km.

We were unable to prove that the AVR was an artifact (though hail moving at horizontal speeds different from the flow in this region may have augmented the AVR), and near-surface winds from a mobile mesonet transect are generally consistent with the presence of the radar-diagnosed AVR. If the AVR is real, it is unclear how common it is in observed supercells and how it would impact tornadogenesis. If the AVR is indeed an artifact, this does not change the conclusion that the Maysville storm lacks a well-defined SVC.

Future observational and modeling studies should continue to examine the SVC. Although this study suggests that an SVC is not necessary for tornadogenesis (at least for brief, weak tornadoes), it is possible that the presence of an SVC may increase the chances of tornadogenesis and modulate tornado strength (as suggested by Orf et al. 2017), as long as it is not coupled with outflow with excessive negative buoyancy. Finally, it is vitally important that observations continue to be collected to verify the realism of results from numerical simulations (especially as the resolution of these simulations increases) and to better understand the spectrum of SVC characteristics. For this reason, the authors are excited to see what insights about SVCs and other internal supercell structures are gleaned from the TORUS field project.

Acknowledgments. The authors thank Drs. Matthew Kumjian and Joshua Wurman for helping in the interpretation of the radar data from the Maysville storm as well as Drs. Erik Rasmussen and Matthew Flournoy for illuminating discussions about the SVC. Dr. David Dowell is acknowledged for writing the radar gridding and dual-Doppler wind synthesis software. All participants in the VORTEX2 field project are also thanked for collecting the data analyzed herein. Finally, we want to extend our sincerest thank

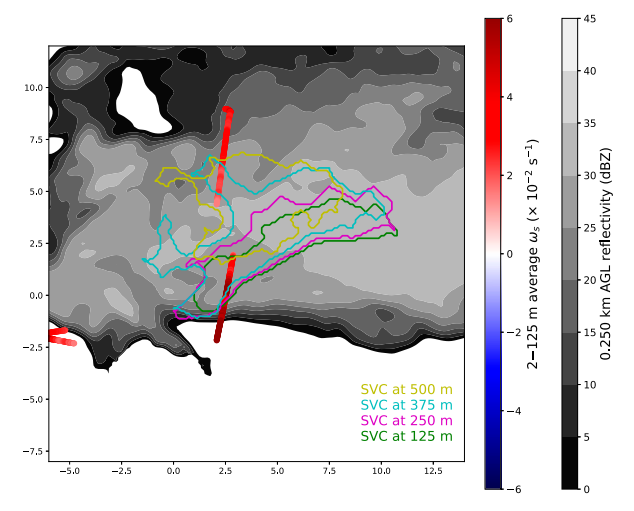


FIG. 15. As in Fig. 14, but for the Prospect Valley storm at 2224: 30 UTC. Green contour denotes the objectively analyzed SVC outline at 125 m AGL and the average streamwise horizontal vorticity (computed using mobile mesonet and dual-Doppler observations) is computed over the 2–125-m layer.

you to Leigh Orf and the two anonymous reviewers whose comments helped improve this manuscript. Funding for this project came from a Pennsylvania State University Graduate Fellowship and the National Science Foundation Graduate Research Fellowship Program under Grant DGE1255832. Figures 1, 4, 6, and 8 were created using the MetPy package in Python (May et al. 2018), and Figs. 9 and 10 were created using the SOLO 3 software package (Oye et al. 1995).

Data availability statement. All data and analysis code used in this study can be found online at the Penn State Data Commons website (https://doi.org/10.26208/xhe7-7e38).

# REFERENCES

Adlerman, E. J., K. K. Droegemeier, and R. Davies-Jones, 1999: A numerical simulation of cyclic mesocyclogenesis. *J. Atmos. Sci.*, **56**, 2045–2069, https://doi.org/10.1175/1520-0469(1999) 056<2045:ANSOCM>2.0.CO;2.

Alexander, C., and J. Wurman, 2008: Updated mobile radar climatology of supercell tornado structures and dynamics. 24th Conf. on Severe Local Storms, Savannah, GA, Amer. Meteor. Soc., 19.4, https://ams.confex.com/ams/pdfpapers/141821.pdf.

Atkins, N. T., E. M. Glidden, and T. M. Nicholson, 2014: Observations of wall cloud formation in supercell thunderstorms during VORTEX2. Mon. Wea. Rev., 142, 4823–4838, https://doi.org/10.1175/MWR-D-14-00125.1.

Barnes, S. L., 1964: A technique for maximizing details in numerical weather map analysis. *J. Appl. Meteor.*, **3**, 396–409, https://doi.org/10.1175/1520-0450(1964)003<0396:ATFMDI>2.0.CO;2.

Beck, J., and C. Weiss, 2013: An assessment of low-level baroclinity and vorticity within a simulated supercell. *Mon. Wea. Rev.*, **141**, 649–669, https://doi.org/10.1175/MWR-D-11-00115.1.

Beck, J. R., J. L. Schroeder, and J. M. Wurman, 2006: High-resolution dual-Doppler analyses of the 29 May 2001 Kress, Texas, cyclic supercell. *Mon. Wea. Rev.*, 134, 3125–3148, https://doi.org/ 10.1175/MWR3246.1. Bowlan, M. A., 2013: Intensification of low-level mesocyclones and associated stormscale evolution in supercell thunderstorms. M.S. thesis, School of Meteorology, University of Oklahoma, 104 pp.

Brandes, E. A., R. P. Davies-Jones, and B. C. Johnson, 1988: Streamwise vorticity effects on supercell morphology and persistence. *J. Atmos. Sci.*, **45**, 947–963, https://doi.org/10.1175/1520-0469(1988)045<0947:SVEOSM>2.0.CO;2.

Coffer, B. E., and M. D. Parker, 2017: Simulated supercells in non-tornadic and tornadic VORTEX2 environments. *Mon. Wea. Rev.*, 145, 149–180, https://doi.org/10.1175/MWR-D-16-0226.1.

—, and —, 2018: Is there a "tipping point" between simulated nontornadic and tornadic supercells in VORTEX2 environments? *Mon. Wea. Rev.*, **146**, 2667–2693, https://doi.org/ 10.1175/MWR-D-18-0050.1.

—, J. M. L. Dahl, L. J. Wicker, and A. J. Clark, 2017: Volatility of tornadogenesis: An ensemble of simulated nontornadic and tornadic supercells in VORTEX2 environments. *Mon. Wea. Rev.*, 145, 4605–4625, https://doi.org/10.1175/MWR-D-17-0152.1.

—, —, R. L. Thompson, B. T. Smith, and R. E. Jewell, 2019: Using near-ground storm relative helicity in supercell tornado forecasting. *Wea. Forecasting*, 34, 1417–1435, https://doi.org/ 10.1175/WAF-D-19-0115.1.

Dahl, J. M. L., 2015: Near-ground rotation in simulated supercells: On the robustness of the baroclinic mechanism. *Mon. Wea. Rev.*, 143, 4929–4942, https://doi.org/10.1175/MWR-D-15-0115.1.

——, M. D. Parker, and L. J. Wicker, 2014: Imported and storm-generated near-ground vertical vorticity in a simulated supercell. *J. Atmos. Sci.*, 71, 3027–3051, https://doi.org/10.1175/JAS-D-13-0123.1.

Davies-Jones, R., 1984: Streamwise vorticity: The origin of updraft rotation in supercell storms. *J. Atmos. Sci.*, **41**, 2991–3006, https://doi.org/10.1175/1520-0469(1984)041<2991: SVTOOU>2.0.CO;2.

——, 2015: A review of supercell and tornado dynamics. *Atmos. Res.*, 158–159, 274–291, https://doi.org/10.1016/j.atmosres.2014.04.007.

—, and H. Brooks, 1993: Mesocyclogenesis from a theoretical perspective. *The Tornado: Its Structure, Dynamics, Prediction,* and Hazards, Geophys. Monogr., Vol. 79, Amer. Geophys. Union, 105–114.

—, D. Burgess, and M. Foster, 1990: Test of helicity as a tornado forecast parameter. Preprints, 16th Conf. on Severe Local Storms, Alberta, Canada, Amer. Meteor. Soc., 588–592.

Doswell, I., and E. N. Rasmussen, 1994: The effect of neglecting the virtual temperature correction on CAPE calculations. *Wea. Forecasting*, **9**, 625–629, https://doi.org/10.1175/1520-0434(1994) 009<0625:TEONTV>2.0.CO;2.

Finley, C., L. Orf, B. Lee, and R. Wilhelmson, 2018: High-resolution simulation of a violent tornado in the 27 April 2011 outbreak environment. *29th Conf. on Severe Local Storms*, Stowe, VT, Amer. Meteor. Soc., 10B.5, https://ams.confex.com/ams/29SLS/webprogram/Paper348812.html.

Grzych, M. L., B. D. Lee, and C. A. Finley, 2007: Thermodynamic analysis of supercell rear-flank downdrafts from project ANSWERS. *Mon. Wea. Rev.*, 135, 240–246, https://doi.org/ 10.1175/MWR3288.1.

Houston, A., B. Argrow, M. C. Coniglio, E. W. Frew, E. N. Rasmussen, C. C. Weiss, and C. L. Ziegler, 2020: Targeted observation by radars and UAS of supercells (TORUS): Summary of the 2019 field campaign. Severe Local Storms Symp., Boston, MA, Amer. Meteor. Soc., 1.3, https://ams.confex.com/ams/2020Annual/meetingapp.cgi/Paper/369999.

Klemp, J. B., and R. Rotunno, 1983: A study of the tornadic region within a supercell thunderstorm. J. Atmos. Sci., 40,

- 359–377, https://doi.org/10.1175/1520-0469(1983)040<0359: ASOTTR>2.0.CO;2.
- Koch, S. E., M. desJardins, and P. J. Kocin, 1983: An interactive Barnes objective map analysis scheme for use with satellite and conventional data. *J. Climate Appl. Meteor.*, 22, 1487–1503, https://doi.org/10.1175/1520-0450(1983)022<1487: AIBOMA>2.0.CO;2.
- Kumjian, M. R., 2013: Principles and applications of dual-polarization weather radar. Part I: Description of the polarimetric radar variables. *J. Oper. Meteor.*, 1, 226–242, https://doi.org/10.15191/ nwajom.2013.0119.
- —, Y. P. Richardson, T. Meyer, K. A. Kosiba, and J. Wurman, 2018: Resonance scattering effects in wet hail observed with a dual-X-band-frequency, dual-polarization Doppler on wheels radar. J. Appl. Meteor. Climatol., 57, 2713–2731, https:// doi.org/10.1175/JAMC-D-17-0362.1.
- Markowski, P. M., and G. H. Bryan, 2016: LES of laminar flow in the PBL: A potential problem for convective storm simulations. *Mon. Wea. Rev.*, 144, 1841–1850, https://doi.org/10.1175/ MWR-D-15-0439.1.
- —, J. M. Straka, and E. N. Rasmussen, 2002: Direct surface thermodynamic observations within the rear-flank downdrafts of nontornadic and tornadic supercells. *Mon. Wea. Rev.*, **130**, 1692–1721, https://doi.org/10.1175/1520-0493(2002)130<1692: DSTOWT>2.0.CO;2.
- —, T. P. Hatlee, and Y. P. Richardson, 2018: Tornadogenesis in the 12 May 2010 supercell thunderstorm intercepted by VORTEX2 near Clinton, Oklahoma. *Mon. Wea. Rev.*, **146**, 3623–3650, https://doi.org/10.1175/MWR-D-18-0196.1.
- May, R., S. Arms, P. Marsh, E. Bruning, and J. Leeman, 2018: MetPy: A Python package for meteorological data. Unidata, accessed 1 October 2019, https://doi.org/10.5065/D6WW7G29.
- Murdzek, S. S., P. M. Markowski, Y. P. Richardson, and R. L. Tanamachi, 2020: Processes preventing the development of a significant tornado in a Colorado supercell on 26 May 2010. *Mon. Wea. Rev.*, 148, 1753–1778, https://doi.org/10.1175/MWR-D-19-0288.1.
- Orf, L., R. Wilhelmson, B. Lee, C. Finley, and A. Houston, 2017: Evolution of a long-track violent tornado within a simulated supercell. *Bull. Amer. Meteor. Soc.*, 98, 45–68, https://doi.org/ 10.1175/BAMS-D-15-00073.1.
- —, A. Dixon, and K. Halbert, 2018: The role of the streamwise vorticity current in tornado genesis and maintenance. 29th Conf. on Severe Local Storms, Stowe, VT, Amer. Meteor. Soc., 1.5, https://ams.confex.com/ams/29SLS/webprogram/ Paper348295.html.
- Oye, R., C. Mueller, and S. Smith, 1995: Software for radar translation, visualization, editing, and interpolation. Preprints, *27th Conf. on Radar Meteorology*, Vail, CO, Amer. Meteor. Soc., 359–361.
- Parker, M. D., 2014: Composite VORTEX2 supercell environments from near-storm soundings. *Mon. Wea. Rev.*, **142**, 508–529, https://doi.org/10.1175/MWR-D-13-00167.1.
- Pauley, P. M., and X. Wu, 1990: The theoretical, discrete, and actual response of the Barnes objective analysis scheme for one- and two-dimensional fields. *Mon. Wea. Rev.*, 118, 1145–1164, https://doi.org/10.1175/1520-0493(1990)118<1145: TTDAAR>2.0.CO;2.
- Rasmussen, E. N., 2003: Refined supercell and tornado forecast parameters. Wea. Forecasting, 18, 530–535, https://doi.org/ 10.1175/1520-0434(2003)18<530:RSATFP>2.0.CO;2.

- Rotunno, R., 1981: On the evolution of thunderstorm rotation. *Mon. Wea. Rev.*, **109**, 577–586, https://doi.org/10.1175/1520-0493(1981) 109<0577:OTEOTR>2.0.CO;2.
- ——, and J. B. Klemp, 1985: On the rotation and propagation of simulated supercell thunderstorms. J. Atmos. Sci., 42, 271–292, https://doi.org/10.1175/1520-0469(1985)042<0271: OTRAPO>2.0.CO;2.
- Schenkman, A. D., M. Xue, and M. Hu, 2014: Tornadogenesis in a high-resolution simulation of the 8 May 2003 Oklahoma City supercell. J. Atmos. Sci., 71, 130–154, https://doi.org/10.1175/ JAS-D-13-073.1.
- Schueth, A., 2018: Comparing observations and simulations of the streamwise vorticity current in a tornadic supercell storm. M.S. thesis, Department of Geoscience, Texas Tech University, 106 pp., https://ttu-ir.tdl.org/handle/2346/74411.
- —, and C. Weiss, 2018: Comparing observations and simulations of the streamwise vorticity current in a tornadic supercell storm. 29th Conf. on Severe Local Storms, Stowe, VT, Amer. Meteor. Soc., 3B.6, https://ams.confex.com/ams/29SLS/webprogram/Paper348686.html.
- —, and —, 2020: How environmental streamwise vorticity modulates the streamwise vorticity current. Severe Local Storms Symp., Boston, MA, Amer. Meteor. Soc., 1.5, https:// ams.confex.com/ams/2020Annual/meetingapp.cgi/Paper/366317.
- Shabbott, C. J., and P. M. Markowski, 2006: Surface in situ observations within the outflow of forward-flank downdrafts of supercell thunderstorms. *Mon. Wea. Rev.*, 134, 1422–1441, https://doi.org/10.1175/MWR3131.1.
- Snyder, J. C., H. B. Bluestein, V. Venkatesh, and S. J. Frasier, 2013: Observations of polarimetric signatures in supercells by an X-band mobile Doppler radar. *Mon. Wea. Rev.*, 141, 3–29, https://doi.org/10.1175/MWR-D-12-00068.1.
- Tanamachi, R. L., H. B. Bluestein, M. Xue, W.-C. Lee, K. A. Orzel, S. J. Frasier, and R. M. Wakimoto, 2013: Near-surface vortex structure in a tornado and in a sub-tornado-strength convective-storm vortex observed by a mobile, W-band radar during VORTEX2. Mon. Wea. Rev., 141, 3661–3690, https:// doi.org/10.1175/MWR-D-12-00331.1.
- Thompson, R. L., R. Edwards, J. A. Hart, K. L. Elmore, and P. Markowski, 2003: Close proximity soundings within supercell environments obtained from the Rapid Update Cycle. *Wea. Forecasting*, **18**, 1243–1261, https://doi.org/10.1175/1520-0434(2003)018<1243:CPSWSE>2.0.CO;2.
- Wang, Y., T.-Y. Yu, A. V. Ryzhkov, and M. R. Kumjian, 2019: Application of spectral polarimetry to a hailstorm at low elevation angle. *J. Atmos. Oceanic Technol.*, 36, 567–583, https://doi.org/10.1175/JTECH-D-18-0115.1.
- Waugh, S., and S. Fredrickson, 2010: An improved aspirated temperature system for mobile meteorological observations, especially in severe weather. 25th Conf. on Severe Local Storms, Denver, CO, Amer. Meteor. Soc., P5.2, https://ams.confex.com/ams/25SLS/techprogram/paper\_176205.htm.
- Weiss, C., A. Schueth, and A. Houston, 2020: TORUS 2019 highlights from the TTUKa mobile Doppler radars. Severe Local Storms Symp., Boston, MA, Amer. Meteor. Soc., 1.4, https:// ams.confex.com/ams/2020Annual/meetingapp.cgi/Paper/366442.
- Wurman, J., D. Dowell, Y. Richardson, P. Markowski, E. Rasmussen, D. Burgess, L. Wicker, and H. B. Bluestein, 2012: The Second Verification of the Origins of Rotation in Tornadoes Experiment: VORTEX2. Bull. Amer. Meteor. Soc., 93, 1147–1170, https://doi.org/10.1175/BAMS-D-11-00010.1.